Nature of the metal-insulator transition in NbO_2

Andrew O'Hara and Alexander A. Demkov*
Department of Physics, The University of Texas at Austin, Austin, Texas 78712, USA
(Received 23 July 2014; revised manuscript received 12 February 2015; published 20 March 2015)

We report a theoretical study of the structural phase transition and associated metal-to-insulator transition in NbO_2 within density functional theory using the transition state theory as formulated in the generalized solid-state nudged elastic band method. Consistent with prior experimental work, we demonstrate that niobium dimerization is primarily driven by soft modes at the P point of the rutile Brillouin zone. In light of our results, it appears that the metal-to-insulator transition in NbO_2 is driven by a second-order structural transition of the Peierls type.

DOI: 10.1103/PhysRevB.91.094305 PACS number(s): 71.30.+h, 64.60.−i

Many oxide materials undergo metal-to-insulator transitions (MITs) as a function of temperature, pressure, and electric field. Applications for such materials include gas sensors [1], window coatings [2], resistive random access memory (RRAM) devices [3], and electronic switches [4–6]. For many electronic applications, it is desirable that the transition temperature be at or above room temperature to isolate field and temperature switching. One promising material receiving much attention is VO_2, which undergoes a metal-to-insulator transition at 340 K [1,7–10]. In VO_2, vanadium atoms are found to dimerize along the c axis of the high-temperature rutile phase suggesting a Peierls type mechanism [7,11–13]. However, given that vanadium is a $3d$ transition metal, the role of strong electron-electron correlations cannot be neglected. Indeed, this metal-to-insulator transition is not just a Peierls distortion, but rather a Mott-Peierls distortion where both effects are needed to correctly describe the insulating ground state [8,14,15]. Furthermore, the proper lattice dynamics for the rutile phase can only be reproduced if correlations are included [16]. This makes the analysis of the transition much more complicated. Niobium dioxide (NbO_2), a sister compound to VO_2, also undergoes a metal-to-insulator transition, albeit at a significantly higher temperature. As niobium is a $4d$, rather than $3d$, transition metal, electron correlations should play a lesser role, making the analysis more tractable. The phase transition in NbO_2 is much less studied, and here we present a first-principles investigation of its mechanism.

NbO_2 undergoes the MIT near 1081 K [17–19] accompanied by a structural transition from an undistorted rutile structure ($P4_2/mnm$) with two formula units per conventional cell shown in Fig. 1(a) to a body-center tetragonal (bct) distorted rutile structure ($I4_1/a$) with 32 formula units per conventional cell [20–22] shown in Fig. 1(b). During this transition, pairs of niobium atoms dimerize along the c axis. The niobium atoms are formally in the Nb^{4+} oxidation state with a valence configuration of $4d^1$. The transition could be purely of the Peierls type, where dimerization between atoms occurs due to the instability associated with a quasi-one-dimensional chain of atoms. However, the precise mechanism of this transition is still not clear. Neutron scattering in single crystal NbO_2 found evidence of a soft phonon mode at the P point, $q_p = (1/4, 1/4, 1/2)$, via critical scattering [23]. Further experiments, however, found no clear evidence for a soft mode at q_p, but rather quasielastic scattering along rods in reciprocal space with an instability near q_p [24]. Classical shell model calculations based on the measured phonon dispersion of TiO_2 and adapted to other rutile structures using Γ mode data found phonon softening at q_p [25]. Analysis of thermodynamic data is mixed, with some indicating that the transition is second order [19] and others reporting that it is first order in nature [26,27]. Previous *ab initio* calculations have shown that density functional theory using augmented spherical waves does qualitatively describe NbO_2 [28] as does plane-wave density functional theory [29]. Here, using transition state theory within density functional theory, we demonstrate that the driving mechanism for the metal-to-insulator phase transition in NbO_2 is primarily structural in nature.

We hypothesize the MIT in NbO_2 to be driven purely by the Peierls instability. To gain insight into the transition mechanism, we search for the minimum energy pathway (MEP) between phases utilizing transition state theory as formulated in the generalized solid-state nudged elastic band (G-SSNEB) method [30] implemented in the VTST extension of the Vienna *ab initio* simulation package (VASP) [31]. The benefit of the G-SSNEB method compared to the standard nudged elastic band method [32,33] is that it allows for cell deformation due to stress and strain in addition to atomic movement between the initial and final phases (in the case of NbO_2, only strain deformations are needed). Our initial cell is taken to be the undistorted bct cell based on the rutile lattice described below, while the final cell is the ground state bct lattice. We employed seven intermediate images initialized by interpolation of the atomic positions and lattice vectors. After convergence, we obtained the MEP between the two phases of NbO_2 and analyzed each intermediate image along the MEP to gain further insight into the mechanism.

We conducted density functional calculations within the local density approximation (LDA) parametrization of Perdew and Zunger [34]. Projector augmented wave pseudopotentials [35,36] were employed with valence configurations of $4p^6 5s^1 4d^4$ for niobium and $2s^2 2p^4$ for oxygen. A plane-wave cutoff energy of 750 eV with $8 \times 8 \times 12$ and $8 \times 8 \times 8$ Γ-centered Monkhorst-Pack grids [37] for rutile and the primitive body-center tetragonal cells, respectively, were used to give convergence of 1 meV per NbO_2 unit for total energy. During relaxation of rutile NbO_2, the first-order

*demkov@physics.utexas.edu

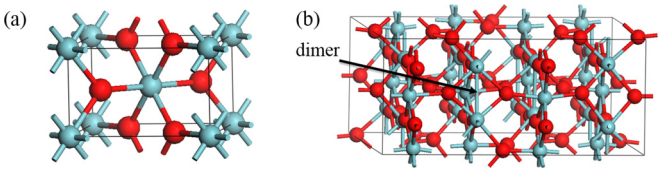

FIG. 1. (Color online) Crystal structure of (a) high-temperature rutile and (b) low-temperature body-center tetragonal phases of NbO_2.

Methfessel-Paxton [38] scheme with a σ value of 0.17 was used for partial occupancies, while the tetrahedron method with Blöchl corrections [39] was used for self-consistent total energy calculations.

The optimized rutile structure for NbO_2 within LDA has $a_R = 4.93$ Å and $c_R = 2.90$ Å versus experimental values of $a_R = 4.8463$ Å and $c_R = 3.0315$ Å [22]. The optimized coordinate for the oxygen atom at the $4f$ Wyckoff position is found to have $u = 0.289$ versus $u = 0.2924$ experimentally. The structural parameters for the LDA calculation of the bct structure are compared against powder neutron data [22] in Table I. Compared to experiment, the lattice constants of $a = 13.64$ Å and $c = 6.01$ Å represent a -0.45% and $+0.45\%$ deviation, respectively, which is typical for such calculations. Furthermore, the calculated niobium-niobium dimer length is 2.70 Å compared with 2.71 Å experimentally. As can be seen from the table, the overall agreement between the theory and experiment is very good.

To use transition state theory, a common cell allowing for a one-to-one mapping of the atoms between phases is needed. The lattice vectors of the rutile and bct cells can be related by $a_1^{\rm bct} \approx 2(a_1^R - a_2^R)$, $a_2^{\rm bct} \approx 2(a_1^R + a_2^R)$, and $a_3^{\rm bct} \approx 2a_3^R$; while the origin for the atomic coordinates is shifted by $(\frac{1}{8}, \frac{1}{8}, 0)$ relative to the bct lattice vectors. Furthermore, a primitive cell of the bct lattice can be generated, which contains half as many NbO_2 units as the conventional cell. The primitive cell lattice vectors are given in terms of the rutile cell vectors as $a_1^{\rm prim} \approx 2a_2^R + a_3^R$, $a_1^{\rm prim} \approx -2a_2^R + a_3^R$, and $a_1^{\rm prim} \approx 2a_1^R - a_3^R$. The lattice vector lengths and atomic positions for this enlarged rutile cell are given in Table I.

In Fig. 2(a), we plot the MEP between the high-temperature and low-temperature phases and band gap as a function of the reaction coordinate (image number). From the energy plot, we see that no barrier exists between the phases indicating that the transition is second order in nature. The enthalpy

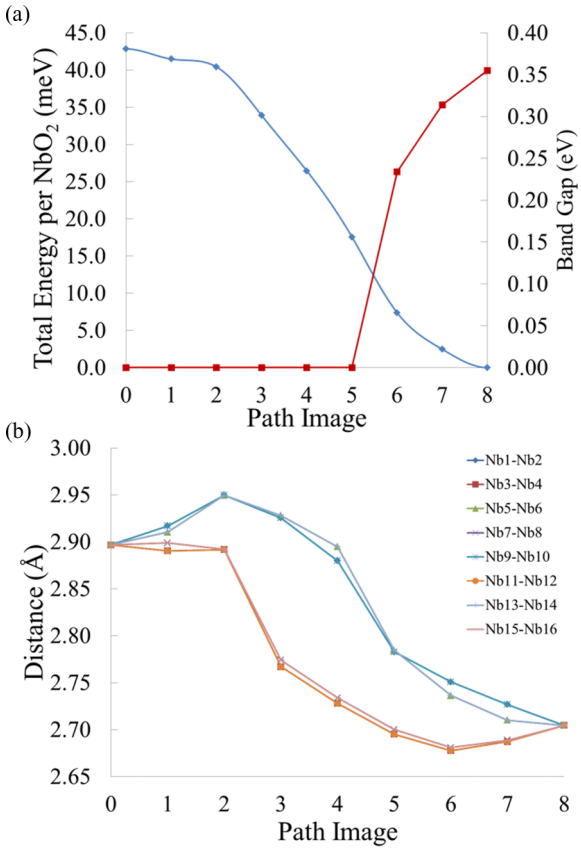

FIG. 2. (Color online) (a) The diamonds show total energy per NbO_2 (the insulating phase is the 0 of energy) with cubic spline interpolation, while the squares show the band gap as a function of G-SSNEB image number. (b) Nb-Nb distance for each pair of dimers tracked through the calculation showing that dimerization occurs on two sublattices.

change between the two phases is 43 meV/NbO_2, similar to experiments ranging from 26.1 to 35.5 meV/NbO_2 [19,26,27]. The calculated electronic density of states (DOS) for each phase [see Fig. 3(a) for rutile and Fig. 3(d) for body-center tetragonal], shows that the rutile phase is metallic with the Fermi energy within the Nb $4d$ t_{2g}-derived bands, while in the bct phase there is a band gap of 0.35 eV. As is common with LDA calculations, this band gap is smaller than recently reported experimental measurements [29,40], however LDA giving a gap strongly suggests that the calculation qualitatively

TABLE I. Comparison of the experimental and LDA-calculated lattice parameters for the body-center tetragonal phase of NbO_2. The last column shows the enlarged rutile cell used for transition state theory calculations.

Parameter	Experimental [22]	Theoretical	Enlarged rutile
Lattice vector a	13.696 Å	13.640 Å	13.943 Å
Lattice vector c	5.981 Å	6.012 Å	5.794 Å
Nb(1) coordinate	(0.116, 0.123, 0.488)	(0.112, 0.122, 0.475)	(0.125, 0.125, 0.500)
Nb(2) coordinate	(0.133, 0.124, 0.031)	(0.132, 0.126, 0.027)	(0.125, 0.125,0.000)
O(1) coordinate	(0.987, 0.133, –0.005)	(0.986, 0.128, –0.021)	(0.980, 0.125, 0.000)
O(2) coordinate	(0.976, 0.126, 0.485)	(0.970, 0.122, 0.509)	(0.980, 0.125, 0.500)
O(3) coordinate	(0.274, 0.119, 0.987)	(0.274, 0.125, 0.000)	(0.270, 0.125, 0.000)
O(4) coordinate	(0.265, 0.126, 0.509)	(0.262, 0.124, 0.502)	(0.270, 0.125, 0.500)

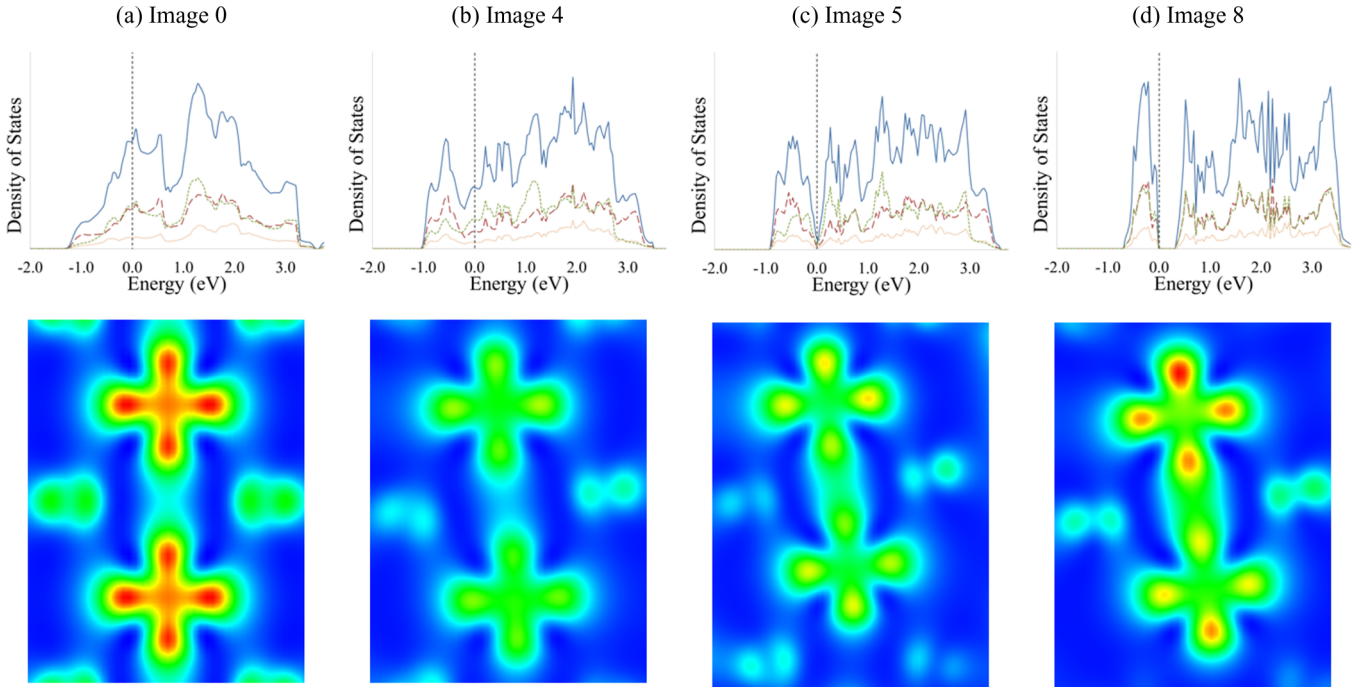

FIG. 3. (Color online) For the Nb1-Nb2 dimer pair, we show the density of states and partial charge density for the occupied d orbitals at (a) the rutile phase (image 0), (b) prior to the large drop in distance (image 4), (c) following the large drop in distance (image 5), and the body-center tetragonal phase (image 8). In the density of states, the solid line is the total density of states, the large dashed line (red) is the site projection for sublattice 1, the small dashed (green) is the site projection for sublattice 2, and the dotted (orange) comes from hybridization of oxygen p orbitals.

describes the ground state correctly. To gain insight into the behavior of the band gap opening, we plot the niobium-niobium distance for all eight pairs of dimerizing Nb atoms. As seen in Fig. 2(b), we can separate the niobium-niobium dimer pairs into two groups: those that show a sharp drop in length of ∼0.12 Å between images 2 and 3 and those that show a similar drop between images 4 and 5. In each case, the change represents almost 60% of the total difference between the niobium-niobium distances in the high- and low-temperature phases. Moreover, the two sets of dimers correspond to splitting the A and B sublattices of niobium atoms in the high-temperature phase such that one of the sublattices has an alternating modulation along the (100) direction and the other along the (010) direction (relative to the rutile lattice). That is, dimerization occurs with half of the A sublattice and half of the B sublattice dimerizing first, followed by the other half of each sublattice (please see Appendix A). By focusing on a specific pair of dimers, we can track the contribution of these atoms to the overall DOS. In Fig. 3, we plot the site projected DOS and charge density of the occupied d states for the rutile phase, predimerization, post-dimerization, and body-center tetragonal phase. Through the phase transition, there is a clear evolution from two separate d_{xy} orbitals on the niobium atoms to a bonding state in which the charge density is shared between the atoms. This can be attributed to the splitting of the pseudo-one-dimensional d_{xy} band in rutile from the other t_{2g} bands to form distinct occupied bonding and unoccupied antibonding states [29]. Because dimerization occurs separately on two different sets of atoms, it is not until all atoms have dimerized that the gap opens for the entire system. Given that $4d$ states are more extended than $3d$ states and that LDA correctly predicts the gap in the ground state, these results strongly suggest that Peierls-type dimerization is indeed the primary mechanism of the transition.

As the G-SSNEB suggests that the phase transition of NbO_2 would, in fact, be a second-order transition, we can gain further insight via Ginzburg-Landau theory [41]. In this approach, the symmetry change is described by an order parameter with a value of zero in the high symmetry phase which becomes nonzero as the system undergoes the transition to lower symmetry. The dimensionality of the order parameter is determined by symmetry. Previous work [21,23] identifies the wave vector $q_p = (1/4, 1/4, 1/2)$ as playing a role in the phase transition. The star of this wave vector, constructed by applying elements of the rutile point group and excluding vectors connected by a reciprocal lattice vector, contains four vectors: $p_1 = (1/4, 1/4, 1/2)$, $p_2 = (1/4, -1/4, 1/2)$, $p_3 = (-1/4, 1/4, 1/2)$, $p_4 = (-1/4, -1/4, 1/2)$; while the symmetry group associated with this k star is C_{2v}. This group has four one-dimensional irreducible representations implying the order parameter is four dimensional. It should be noted the order parameter of VO_2 is also four dimensional, but due to different symmetry arguments [42]. For structural phase transitions, the order parameter represents a set of displacements that connect the phases; therefore, it should be possible to use the distortions for each of these P points as components of the order parameter.

Using the forces calculated by VASP converged to 10^{-4} eV/Å and the harmonic approximation as implemented in Ref. [43] with a $3 \times 3 \times 5$ supercell, we calculate the

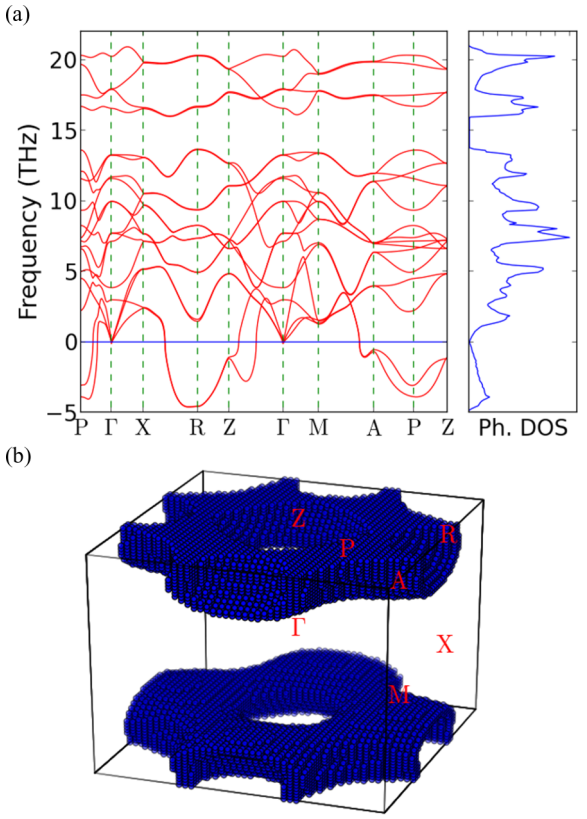

FIG. 4. (Color online) (a) The phonon density of states for NbO_2 calculated within the harmonic approximation showing a peak in the soft mode density at $3.89i$ THz. (b) Plot of the wave vectors within the Brillouin zone in a window of $4.09i$ to $3.69i$ THz showing the origin of this peak.

phonon dispersion of NbO_2 and find soft modes around the Z, A, R, and P points of the Brillouin zone (BZ) [44]. The calculated Debye temperature was determined to be 608 K which is similar to the measured low-temperature phase's Debye temperature measured to be between 588 and 596 K [45–47]. Plotting the phonon DOS [Fig. 4(a)], we notice a peak in the soft mode DOS around $f = 3.89i$ THz. In Fig. 4(b) we plot the k vectors associated with the frequency window from $4.09i$ to $3.68i$ and find that these modes are primarily in the vicinity of the P point. Furthermore, we can project the initial displacement of the G-SSNEB onto each soft mode eigenvector to determine the relative importance of each soft mode (please see Appendix B). For each of the displacement vectors at the Z, A, and R type points (including each possible wave vector on the $(k_x, k_y, \frac{1}{2})$ plane and both imaginary frequencies at each point), the overlaps range between 0.0 and 0.07 in magnitude. However, at each of the P points, the displacement vector for the upper soft phonon branch are 0.19, 0.13, −0.02, and 0.35 confirming the importance of the P point determined in experiment [23,24] compared to Z, A, and R points. Furthermore, as the P point displacements should be able to represent the order parameter, it is interesting to note that the soft mode vectors at the P point obey the following mappings under the generators of the rutile space group, denoting the four vectors p_1, p_2, p_3, p_4 as 1,2,3,4: (1234) goes to $(4\bar{3}21)$ for C_{2z}; $(\bar{3}1\bar{4}2)$ for $(C_{4z}|\frac{1}{2},\frac{1}{2},\frac{1}{2})$, $(\bar{2}143)$ for $(C_{2y}|\frac{1}{2},\frac{1}{2},\frac{1}{2})$, and is negated for inversion. Mukamel discussed that either the A_1 or A_2 irreducible representation of C_{2v} was responsible for the phase transition in NbO_2 [48]. Using the multiplier representation [49], Pynn *et al.* [21] constructed the expected form of the polarization basis vector for p_1 displacements and concluded that A_1 (S_1 in their notation) was responsible. Using their construction, we however find that the upper soft phonon branch, which matches our G-SSNEB calculation, takes the form of their A_2 vector (S_4 in their notation, S_2 in the notation Ref. [50]). Our lower soft phonon branch matches their A_1 vector's form.

In summary, our results indicate that the MIT of NbO_2 is driven by a second-order structural transition of the Peierls type via dimerization of chains of Nb atoms. We have studied the structural phase transition within density functional theory using transition state theory. Furthermore, we demonstrate that dimerization alone (as opposed to strong electron correlation effects) is responsible for opening the band gap after all pairs of niobium atoms have dimerized. Analyzing the phonon dispersion together with the transition path, we identify the soft phonon modes of the high-temperature metallic phase primarily associated with Nb dimerization. In agreement with prior experimental work [21,23,24], the importance of the P point wave vector has been confirmed theoretically. In addition, our results suggest that additional modes in the vicinity of the P point may also play a role as predicted in Ref. [24]. Our work shows, that unlike in VO_2, the phase transition in NbO_2 can be described by a purely structural transition.

This work is supported by the Semiconductor Research Corporation Contract 2013-VJ-2299 and the Texas Advanced Computing Center (TACC). We thank Ilya Karpov for useful discussions and Richard Hatch and Chungwei Lin for their help in preparing this manuscript.

APPENDIX A: IDENTIFYING THE TWO SUBLATTICES FOR DIMERIZATION

In Fig. 2(b) of the main text, it is shown that there are two sublattices of the NbO_2 primitive cell that dimerize at separate points along the G-SSNEB path. In this Appendix, we show explicitly how these two sublattices result from a modulation of the A and B sublattices of the niobium atoms in the rutile phase. In Fig. 5, the first group of atoms to dimerize is represented

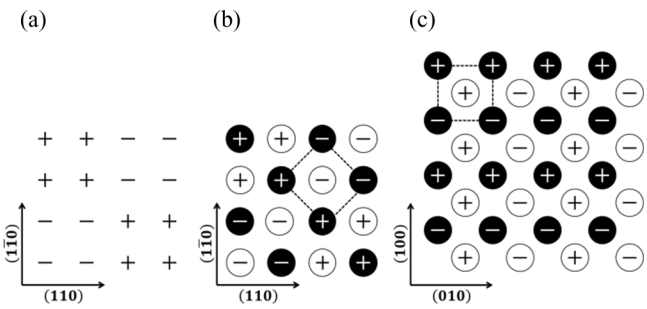

FIG. 5. This figure lays out the three steps to relate (a) the observed dimerization pattern via (b) labeling and rotation to (c) the pattern in the initial rutile cell.

by a "+"; while the second group of atoms to dimerize is represented by a "−." Furthermore, the A sublattice of the high-temperature rutile lattice is represented by a closed circle (•) and the B sublattice by an open circle (○). In all cases, the figures are assumed to be looking along the (001) direction. First [Fig. 5(a)], we show how the two sets of sublattices appear in the low-temperature cell of NbO_2 (directions used are relative to the rutile cell, which the low-temperature cell is rotated 45° with respect to). The next step [Fig. 5(b)] is to label the atoms that are representative of the A and B sublattices. Furthermore, we show how the rutile lattice sits within this pattern. The final step [Fig. 5(c)] is to undo the rotation of the low-temperature cell so that we are explicitly aligned along the (100) and (010) directions of the rutile lattice (we also enlarge the number of included atoms for clarity). From this final figure, the 90° rotated modulations of the A versus B sublattices become readily apparent. Furthermore, it should be noted that these modulation patterns also obey the screw axis that transforms the A sublattice to the B sublattice.

APPENDIX B: CALCULATING THE PROJECTION BETWEEN G-SSNEB AND SOFT MODE DISPLACEMENTS

In the main text, we discuss the projection of the G-SSNEB initial displacement onto the displacements for each of the soft modes found from the phonon calculation. We define the initial displacement of the G-SSNEB calculation χ as the difference between the atomic positions at image 0 and image 1. For a given wave vector and soft mode frequency, the eigenvector of the dynamical matrix gives the associated distortion for the six-atom rutile cell. Using the Bloch theorem and our cell mappings, we can extend the displacement vector to include each atom in our undistorted primitive body-center tetragonal cell, yielding an overall displacement vector ν. Therefore, we have our displacement vector for the initial distortion (G-SSNEB calculation) and a displacement vector for a soft mode at any wave vector, both of which contain 144 entries ($3N$). In order to determine which are primarily responsible for the transition, we compute the projection of the G-SSNEB displacement onto the soft mode displacement as $\frac{\chi \cdot \nu}{\|\chi\| \|\nu\|}$.

[1] E. Strelcov, Y. Lilach, and A. Kolmakov, Nano Lett. **9**, 2322 (2009).
[2] T. D. Manning, I. P. Parkin, M. E. Pemble, D. Sheel, and D. Vernardou, Chem. Mater. **16**, 744 (2004).
[3] S. Kim, J. Park, J. Woo, C. Cho, W. Lee, J. Shin, G. Choi, S. Park, D. Lee, B. H. Lee, and H. Hwang, Microelectron. Eng. **107**, 33 (2013).
[4] S. H. Shin, T. Halpern, and P. M. Raccah, J. Appl. Phys. **48**, 3150 (1977).
[5] W. L. Lim, E. J. Moon, J. W. Freeland, D. J. Meyers, M. Kareev, J. Chakhalian, and S. Urazhdin, Appl. Phys. Lett. **101**, 143111 (2012).
[6] Z. Yang, C. Ko, and S. Ramanathan, Annu. Rev. Mater. Res. **41**, 337 (2011).
[7] A. Cavalleri, T. Dekorsy, H. Chong, J. Kieffer, and R. Schoenlein, Phys. Rev. B **70**, 161102 (2004).
[8] S. Biermann, A. Poteryaev, A. I. Lichtenstein, and A. Georges, Phys. Rev. Lett. **94**, 026404 (2005).
[9] M. M. Qazilbash, M. Brehm, B.-G. Chae, P.-C. Ho, G. O. Andreev, B.-J. Kim, S. J. Yun, A. V Balatsky, M. B. Maple, F. Keilmann, H.-T. Kim, and D. N. Basov, Science **318**, 1750 (2007).
[10] A. C. Jones, S. Berweger, J. Wei, D. Cobden, and M. B. Raschke, Nano Lett. **10**, 1574 (2010).
[11] J. B. Goodenough, J. Solid State Chem. **3**, 490 (1971).
[12] R. M. Wentzcovitch, Phys. Rev. Lett. **72**, 3389 (1994).
[13] R. Wentzcovitch, W. Schulz, and P. Allen, Phys. Rev. Lett. **73**, 3043 (1994).
[14] M. W. Haverkort, Z. Hu, A. Tanaka, W. Reichelt, S. V. Streltsov, M. A. Korotin, V. I. Anisimov, H. H. Hsieh, H.-J. Lin, C. T. Chen, D. I. Khomskii, and L. H. Tjeng, Phys. Rev. Lett. **95**, 196404 (2005).
[15] C. Weber, D. D. O'Regan, N. D. M. Hine, M. C. Payne, G. Kotliar, and P. B. Littlewood, Phys. Rev. Lett. **108**, 256402 (2012).
[16] S. Kim, K. Kim, C.-J. Kang, and B. I. Min, Phys. Rev. B **87**, 195106 (2013).
[17] R. Janninck and D. Whitmore, J. Phys. Chem. Solids **27**, 1183 (1966).
[18] R. Pynn and J. D. Axe, J. Phys. C Solid State Phys. **9**, L199 (1976).
[19] K. Seta and K. Naito, J. Chem. Thermodyn. **14**, 921 (1982).
[20] A. K. Cheetham and C. N. R. Rao, Acta Crystallogr. Sect. B **32**, 1579 (1976).
[21] R. Pynn, J. Axe, and R. Thomas, Phys. Rev. B **13**, 2965 (1976).
[22] A. A. Bolzan, C. Fong, B. J. Kennedy, and C. J. Howard, J. Solid State Chem. **113**, 9 (1994).
[23] S. M. Shapiro, J. D. Axe, G. Shirane, and P. M. Raccah, Solid State Commun. **15**, 377 (1974).
[24] R. Pynn, J. Axe, and P. Raccah, Phys. Rev. B **17**, 2196 (1978).
[25] F. Gervais and W. Kress, Phys. Rev. B **31**, 4809 (1985).
[26] C. N. R. Rao, G. R. Rao, and G. V. S. Rao, J. Solid State Chem. **6**, 340 (1973).
[27] K. T. Jacob, C. Shekhar, M. Vinay, and Y. Waseda, J. Chem. Eng. Data **55**, 4854 (2010).
[28] V. Eyert, Europhys. Lett. **58**, 851 (2002).
[29] A. O'Hara, T. N. Nunley, A. B. Posadas, S. Zollner, and A. A. Demkov, J. Appl. Phys. **116**, 213705 (2014).
[30] D. Sheppard, P. Xiao, W. Chemelewski, D. D. Johnson, and G. Henkelman, J. Chem. Phys. **136**, 074103 (2012).
[31] G. Kresse and J. Furthmüller, Phys. Rev. B **54**, 11169 (1996).
[32] G. Henkelman, B. P. Uberuaga, and H. Jonsson, J. Chem. Phys. **113**, 9901 (2000).
[33] G. Henkelman and H. Jonsson, J. Chem. Phys. **113**, 9978 (2000).
[34] J. Perdew and A. Zunger, Phys. Rev. B **23**, 5048 (1981).
[35] P. Blöchl, Phys. Rev. B **50**, 17953 (1994).
[36] G. Kresse and D. Joubert, Phys. Rev. B **59**, 1758 (1999).
[37] H. Monkhorst and J. Pack, Phys. Rev. B **13**, 5188 (1976).
[38] M. Methfessel and A. Paxton, Phys. Rev. B **40**, 3616 (1989).

[39] P. Blöchl, O. Jepsen, and O. Andersen, Phys. Rev. B **49**, 16223 (1994).
[40] A. B. Posadas, A. O'Hara, S. Rangan, R. A. Bartynski, and A. A. Demkov, Appl. Phys. Lett. **104**, 092901 (2014).
[41] L. D. Landau, E. M. Lifshitz, and L. P. Pitaevski, *Statistical Physics Part 1*, 3rd ed. (Pergamon, New York, 1980).
[42] A. Tselev, I. A. Luk'yanchuk, I. N. Ivanov, J. D. Budai, J. Z. Tischler, E. Strelcov, A. Kolmakov, and S. V Kalinin, Nano Lett. **10**, 4409 (2010).
[43] A. Slepko and A. A. Demkov, J. Appl. Phys. **117**, 074701 (2015).
[44] Employing the Euclidean metric for the harmonic matrix gives a norm of 3.15, while applying the same norm to the anharmonicity (obtained by not averaging positive and negative displacements) yields 0.10 at Γ (and smaller at *P*). As such, the anharmonicity introduces a fairly small perturbation to the optical modes. Furthermore, while the phase is stable above the Debye temperature, such an approach has commonly been shown to be applicable (such as the case of HfO_2).
[45] W. Boyle, J. Bennett, S. Shin, and R. Sladek, Phys. Rev. B **14**, 526 (1976).
[46] J. G. Bennett and R. J. Sladek, Solid State Commun. **25**, 1035 (1978).
[47] A. Wu and R. Sladek, Phys. Rev. B **26**, 2159 (1982).
[48] D. Mukamel, Phys. Rev. Lett. **34**, 481 (1975).
[49] A. Maradudin and S. Vosko, Rev. Mod. Phys. **40**, 1 (1968).
[50] R. S. Katiyar, J. Phys. C Solid State Phys. **3**, 1087 (1970).